Proceedings of the 14th International Pipeline Conference

IPC2018
September 24-28, 2018, Calgary, Alberta, Canada

IPC2018-78631

SIMULATION OF A FULL-SCALE CO_2 FRACTURE PROPAGATION TEST

Gaute Gruben
SINTEF Industry
Trondheim, Norway

Stephane Dumoulin
SINTEF Industry
Trondheim, Norway

Håkon Nordhagen
SINTEF Industry
Trondheim, Norway

Morten Hammer
SINTEF Energy Research
Trondheim, Norway

Svend T. Munkejord
SINTEF Energy Research
Trondheim, Norway

ABSTRACT

In this study, we present results from a numerical model of a full-scale fracture propagation test where the pipe sections are filled with impure, dense liquid-phase carbon dioxide. All the pipe sections had a 24" outer diameter and a diameter/thickness ratio of ~32. A near symmetric telescopic set-up with increasing toughness in the West and East directions was applied.

Due to the near symmetric conditions in both set-up and results, only the East direction is modelled in the numerical study. The numerical model is built in the framework of the commercial finite element (FE) software LS-DYNA. The fluid dynamics is solved using an in-house computational fluid dynamics (CFD) solver which is coupled with the FE solver through a user-defined loading subroutine. As part of the coupling scheme, the FE model sends the crack opening profile to the CFD solver which returns the pressure from the fluid. The pipeline is discretized by shell elements, while the backfill is represented by the smoothed-particle hydrodynamics (SPH) method. The steel pipe is described by the J_2 constitutive model and an energy-based fracture criterion, while the Mohr-Coulomb material model is applied for the backfill material. The CFD solver applies a one-dimensional homogeneous equilibrium model where the thermodynamic properties of the CO_2 are represented by the Peng-Robinson equation-of-state (EOS).

The results from the simulations in terms of crack velocity and pressure agree well with the experimental data for the low and medium toughness pipe sections, while a conservative prediction is given for the high-toughness section. Further work for strengthening the reliability of the model to predict the arrest vs. no-arrest boundary of a running ductile fracture is addressed.

INTRODUCTION

The design of pipelines for arresting running ductile fracture (RDF) has for several decades been based on the work conducted at the Battelle Memorial Institute in the 1960s and 70s. This work culminated in the semi-empirical Battelle Two Curve Method (BTCM) [1]. The BTCM was developed for fluids in gas phase prior to and after decompression, and the empirical dataset was based on steel pipes with what is now considered very low toughness. Empirical correction factors have later been introduced to adjust the needed Charpy V-notch (CVN) energy to arrest running fracture in higher toughness steel pipes as predicted by the BTCM [2, 3]. However, it has been shown that when the escaping fluid is two-phase CO_2, the BTCM method is non-conservative, even with the high toughness CVN correction [4]. More recently, it has been shown that a correction on the arrest pressure given by the BTCM is more promising than a correction on the required CVN energy for arrest [5]. This type of correction has found its way into codes such as ISO 27913 [6] and DNVGL-RP-F104 [7]. However, the available data for CO_2 full-scale burst tests are scarce, and so determining appropriate correction factors is challenging [8].

Several numerical approaches have been established to predict conditions for crack arrest in pipelines. They can be divided into three main categories: (i) an advanced fluid mechanics approach coupled with a simplified structural mechanics approach [9], (ii) a simplified fluid mechanics approach coupled with an advanced structural mechanics approach [10-12] and (iii) an advanced fluid mechanics approach coupled with an advanced structural mechanics approach [13, 14]. In the advanced fluid mechanics approaches, a CFD code is used, while in the simplified ones, simple expressions are used for the pressure decay. In the advanced structural mechanics approaches, the FE method is used in conjunction with advanced models for fracture such as the Gurson-Tvergaard-Needleman model [10, 11] or the cohesive zone model [10-14] while in the simplified ones the crack tip opening angle approach [14], or BTCM [9] is used. In all approaches, backfill is either accounted

for in a simplified manner or not at all. Note that all, but a few of the works done concern natural gas. There is, to the authors' knowledge, no approach explicitly discretizing the pipe, the fracture propagation, the fluid as well as the backfill, neither for natural gas nor CO_2. Note Shibanuma et al. [15] who use a 1D finite difference method for both the fluid and the structure.

Full-scale crack arrest testing can be applied in design of new pipelines, but in requalification of an existing pipeline, this approach is more challenging. An accurate and reliable model to predict crack arrest is clearly of interest. A model is always a simplification of the physical phenomena, but analytical models of the type typically found in design codes are in general more simplified than models used in computational mechanics. As for computational mechanics models addressing the RDF problem, DNVGL-RP-F104 [7] states 'Further R&D work is required to develop validated and robust numerical methodologies for prediction of running ductile fracture, and of decompression flow in CO_2 pipelines in the case of running ductile fracture'. In this study we aim to increase the reliability of the coupled FE–CFD code developed at SINTEF [16-18], by, for the first time, performing a simulation of a *full-scale* CO_2 crack arrest test and compare the results with experimental data. The COOLTRANS full-scale Test 03 is chosen here, since in this test, the pipe is relatively short compared to other full-scale tests, which is practical with respect to computational time.

EXPERIMENTAL

The experimental campaign was presented by Cosham et al. in [5]. However, some of the most important aspects regarding the present study are repeated here. The experiment, i.e. Test 03, was conducted on pipe sections of Grade L450 with nominally 610 mm (24 inch) outer diameter and 19.1 mm (0.75 inch) wall thickness. A telescopic set-up with increasing CVN energies was applied, as shown in Figure 1. High-toughness sections 3W and 3E and pipe reservoirs with a length of approximately 115 m in each direction were part of the set-up, but are not shown in Figure 1. The length of the reservoirs ensured that the propagating crack was not influenced by reflected waves. The initial pressure of the CO_2 was 150.2 barg and the pressure plateau after depressurization was reached at ~89 barg and gradually decreased as shown in Figure 2. A quaternary mixture of carbon dioxide (90.3 mol-%), hydrogen (1.1 mol-%), nitrogen (6.6 mol-%) and oxygen (2.0 mol-%) was used[1]. The initial temperature was 15°C. At the crack-tip the expected saturation pressure was 81–83 barg.

The pipe was buried in the native boulder clay to a depth of 1.2 m to the top of the pipe. The conditions in terms of loading, boundary conditions and material in the East and West directions were similar, thus making this a near symmetric set-up. This was also reflected in the results; the pressure, the crack-velocity and the final axial crack length were similar in both directions. The crack propagated through the initiation pipe (marked 2 in Figure 1) with a maximum speed of 130 m/s before it propagated through the first test pipes 1W and 1E at ~100 m/s and arrested immediately in the higher toughness test pipes 2W and 2E. The axial crack length was approximately 16 m in both directions.

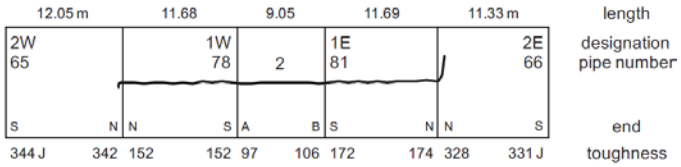

Figure 1 The telescopic set-up and the crack-path from the COOLTRANS full-scale Test 03. Bottom numbers indicate CVN energies in pipe sections. Taken from [5].

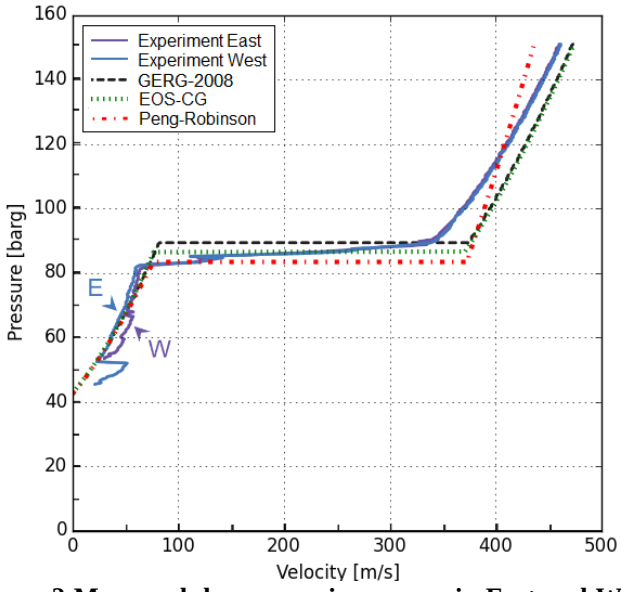

Figure 2 Measured decompression curves in East and West directions and predicted decompression curves with the GERG-2008 EOS [19], the EOS-CG [20] and the Peng-Robinson EOS [21].

NUMERICAL MODELLING

The numerical model is built with the SINTEF coupled FE-CFD code [16-18], where a finite element (FE) solver is coupled with a computational fluid dynamics (CFD) solver. To our knowledge this is the only numerical model which couples a full 3D structural solver with a CFD solver for CO_2. In the following, the numerical scheme is outlined before firm model data, parameter identification and results are presented.

Coupled FE-CFD code overview

The FE-CFD model is built in the framework of the commercial FE software LS-DYNA [22] and coupled with an in-house CFD solver through a user-defined loading subroutine. The deformations in the steel pipe and the surrounding soil are

[1] Table 2 in Cosham et al., 2016 [5], and Table 6 in Cosham et al., 2014 [4] contain a typographical; Tests 02 and 03 contained oxygen, not methane [A. Cosham, 2018, Private communication].

calculated in LS-DYNA using a Lagrangian formulation. The steel pipe is discretized with shell elements. The surrounding backfill is discretized using smoothed particle hydrodynamics (SPH). The pressure of the escaping fluid downstream the crack-tip and the expansion wave upstream the crack-tip are calculated by the CFD solver based on a one-dimensional Eulerian grid. A routine for estimating the pressure profiles in the cross-sections on the flaring flaps downstream the crack-tip is applied [17]. To ease the mapping of the pressure profiles to the FE solver, the shell element discretization in the longitudinal direction of the pipe is coherent with the CFD grid. The complete mechanical system with structure, load and boundary conditions are included in the conservation of momentum equation, which for all the degrees-of-freedom (DOF) in the FE model for each time increment, *n*, is given as

$$\mathbf{M}\ddot{\mathbf{u}}^n + \mathbf{C}\dot{\mathbf{u}}^n + \mathbf{R}_{\text{int}}^n = \mathbf{R}_{\text{ext}}^n \qquad (1)$$

where $\mathbf{M}$ and $\mathbf{C}$ are the system mass and damping matrices, $\ddot{\mathbf{u}}^n$ and $\dot{\mathbf{u}}^n$ are vectors representing respectively the acceleration and the velocity of the DOFs. The vector $\mathbf{R}_{\text{int}}^n$ represents the internal forces from the shell elements and the SPH particles for each DOF, while $\mathbf{R}_{\text{ext}}^n$ represents the external forces acting on the system DOF from the fluid inside the pipe and the contact interaction between the SPH particles and the shell elements. The half-step Central Difference Method is applied to solve Eq. (1), and for each time increment, *n*:

1. The calculated loading $\mathbf{R}_{\text{ext}}^n$ and the internal forces $\mathbf{R}_{\text{int}}^n$ are used to calculate the accelerations $\ddot{\mathbf{u}}^n$,
2. The velocities, $\dot{\mathbf{u}}^n$, and displacements, $\mathbf{u}^n$, of the DOFs are found from integration of $\ddot{\mathbf{u}}^n$,
3. The displacements, $\mathbf{u}^n$, are used as input to the CFD solver to establish $\mathbf{R}_{\text{ext}}^{n+1}$,
4. The internal forces, $\mathbf{R}_{\text{int}}^{n+1}$, are calculated from $\mathbf{u}^n$, $\dot{\mathbf{u}}^n$ and $\mathbf{R}_{\text{ext}}^{n+1}$.

Material model

The internal forces $\mathbf{R}_{\text{int}}^n$ are calculated from the response of the steel and soil material models and specific element/SPH features such as hourglass stiffness and element deletion, i.e. the effect of simulating an expanding crack on the mechanical system goes through $\mathbf{R}_{\text{int}}^n$. The soil material is described by the Mohr-Coulomb (M-C) model as detailed in [18]. The steel pipe material is described by a rate dependent J_2 formulation, and onset of fracture is modelled by the Cockcroft-Latham (CL) criterion following a user-defined material subroutine. The flow stress is defined as

$$\sigma_f = \left[\sigma_0 + \sum_{i=1}^{2} Q_i\left(1-\exp\left(-\frac{\theta_i}{Q_i}p\right)\right)\right]\left(1-\frac{\dot{p}}{\dot{p}_0}\right)^c\left[1-\left(\frac{T-T_0}{T_0-T_m}\right)^m\right] \qquad (2)$$

where $\dot{p}$ is the equivalent plastic strain-rate and $p=\int \dot{p}\,dt$ is the equivalent plastic strain, σ_0 is the initial yield stress, Q_i and C_i are parameters governing the work hardening, whereas c and $\dot{p}_0$ are parameters controlling the strain rate sensitivity. The material temperature is given by *T*, while T_0 is the reference temperature, T_m is the melting temperature and *m* is an exponent controlling the temperature influence on the flow stress. It is assumed that 90% of the plastic work is adiabatically converted to heat, thus the Taylor-Quinney coefficient is set to 0.9. The CL fracture criterion is expressed as

$$W=\int_0^p \langle\sigma_1\rangle\,dp \le W_C, \quad \langle\sigma_1\rangle = \max(\sigma_1, 0) \qquad (3)$$

where W_C is the fracture parameter and σ_1 is the major principal stress. As W_C is reached in one integration point, the element loses its deviatoric strength and does not contribute to $\mathbf{R}_{\text{int}}^n$. The propagating crack is thus treated as a series of fracture initiation in the elements along the crack path. The fracture criterion is only applied in a seam of elements along the pipe length. A consequence of pre-determining the crack-path is that ring-off is not captured in the model. If the crack velocity goes beneath a predefined value, crack arrest is assumed and the simulation is terminated.

Fluid model

The external forces $\mathbf{R}_{\text{ext}}^n$ stem from the pressure of the fluid inside the pipe and the contact interaction between the SPH particles and the shell elements. It is noted that only the kinetic effect of the fluid on the steel pipe is included in Eq. (1), momentum of the fluid is not included. Further, the stable time step in the FE solver is smaller than the stable time step in the CFD solver. Hence, in our simulations, the FE solver takes several steps for each time $\mathbf{R}_{\text{ext}}^n$ is updated from the CFD solver. The one-dimensional fluid model calculates two pressures at each axial computational cell: the cross-sectional average pressure p_{av}, and the escape pressure p_e. The latter is only calculated downstream the crack-tip. To calculate p_{av} and p_e, a homogeneous equilibrium model is employed. In this multiphase flow model, it is assumed that the phases have the same temperature, pressure, chemical potential and velocity. The governing equations will then have the same form as the Euler equations for single-phase compressible inviscid flow, consisting of a mass-conservation equation, a momentum-balance equation and a balance equation for the total energy. The thermodynamic properties of the mixture are calculated using the Peng-Robinson EOS [21], employing classical van der Waals mixing rules and symmetric binary interaction parameters, see also [23]. For the fluid behavior upstream the propagating crack tip, where no circumferential variation in pressure is observed experimentally, the average pressure, p_{av}, is applied to all elements corresponding to each fluid computational cell in the structure model. Downstream the crack tip, the circumferential pressure variation

is modelled using a pressure-profile reconstruction. Here, an additional estimate is performed for the vertical flow at each axial position which depends on the size of the pipe opening. Since the CO_2 mixture is going through a phase change during the outflow, the common assumption of ideal gas cannot be used. The outflow is calculated as quasi-steady isentropic compressible Bernoulli flow in a variable cross-section. The escape pressure is usually not the ambient pressure due to the phenomenon of choked flow. Because the flow is assumed to be steady and adiabatic, a simple form of choked flow theory is employed, which states that the escape velocity cannot exceed the local speed of sound at the point of escape.

More details on the CFD model and the pressure-profile reconstruction are found in [17], although in the present work, we employed a second-order method for the CFD solver. It is a semi-discrete monotone upwind-centered scheme for conservation laws (MUSCL) along with a second-order strong-stability-preserving Runge–Kutta method. See [24] for details.

Geometry, discretization and boundary conditions

Since the full-scale crack arrest test had a near symmetric set-up, only the East direction was modelled. Further, only the sections exposed to the propagating crack in the experiment were modelled, i.e. section 3E and the reservoir sections are not included in the model. The sections and the surrounding soil of the full-scale model are shown in Figure 3(a). In the CFD code, non-reflecting boundary conditions were applied at the end of section 2E, since the fracture was not influenced by the reflected decompression wave in the experiment. For both the CFD model and the FE model, symmetric boundary conditions were applied at the cross section in the centre of the pipeline (left side in Figure 3(a)). Initial simulations showed that modelling the native boulder clay with an SPH particle density equal to 6 particles over the pipe outer diameter (OD) gave converged results. Based on previous experience, SPH particles were applied in a region corresponding to 2.5 OD from the pipe wall on the sides and beneath the pipe, giving a total height of 3.3 m and a total width of 3.6 m of the modelled clay, see Figure 3(c). The shell elements discretizing the pipe sections had a thickness of 19.3 mm, 19.2 mm and 19.5 mm for section I (initiation section), 1E and 2E, respectively as measured in the experiments. Along the crack-seam, the initial element size was 20 mm in the longitudinal direction and 9.5 mm in the hoop direction. The in-plane element size is related to the thickness of the pipe wall, which in turn is related to the width of the necking instability as discussed in [18]. The remainder of the shell mesh has an in-plane size of 20 mm x 20 mm. A shorter model was also studied. In this model, 5.1 m (8.3 OD) of section 1E was included in addiction to section 2E, see Figure 3(c). The motivation for the 'Short' model was (1) to see if the predicted propagation and arrest in the last two sections are captured with a smaller model with significantly smaller computational costs, and (2) to perform an initial sensitivity study.

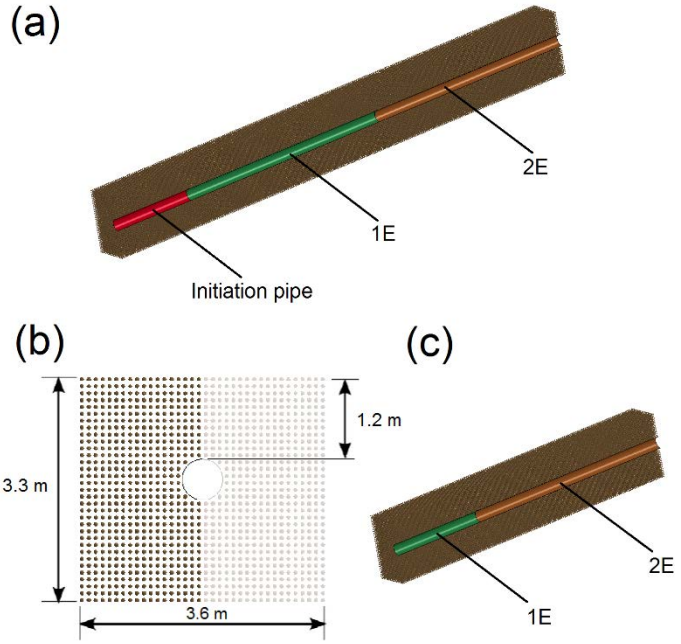

Figure 3 (a) Geometry of the sections and surrounding soil in the full-scale model of the east direction. Half the model is blanked out for visualization. (b) Dimensions of the soil cross-section. The SPH particles blanked out in (a) and (c) are illustrated with lighter color. (c) Geometry of the 'Short' model.

Material parameter identification

The experimental material parameters for the pipe sections were given in [5] as yield strength (*YS*), tensile strength (*TS*), Charpy V-notch energy (CVN) and Drop-Weight-Tear-Test energy (DWTT). In this study the calibration procedure presented in [18] is applied, thus using *YS*, *TS* and CVN as input parameters. Only the material of the pipe sections in the East direction are calibrated. Table 1 summarizes *YS*, *TS* and CVN as an average of the values collected from both ends in each pipe section. It is noted that the three materials can be classified as low-toughness (section I), medium toughness (section 1E) and high-toughness (section 2E). An estimate of the true stress-strain relation is found using the empirical method proposed by Liessem et al. [25]. Here the flow stress is described by Hollomon's equation as $\sigma_f = A \cdot p^n$ and the parameters A and n are estimated as

$$n = 0.151\left(\ln\left(2-\tfrac{YS}{TS}\right)\right)^{0.461} + 0.575\left(\ln\left(2-\tfrac{YS}{TS}\right)\right)^{1.61} \quad (4)$$

$$A = TS\left(\tfrac{e}{n}\right)^n, \quad e = 2.71828... \quad (5)$$

The least squares method is applied to fit the Voce hardening parameters to the hardening curve determined by the Hollomon equation for each pipe material. The Hollomon and Voce parameters are given in Table 1, and the estimated flow stress curves are shown in Figure 4. The strain-rate sensitivity of the pipe section materials is assumed to be similar to the X65 steel

investigated in [16], i.e. $c = 0.015$ and $\dot{p}_0 = 0.011/\mathrm{s}$. The adiabatic heating of the steels is modelled with a reference temperature $T_0 = 293$ K, melting temperature $T_m = 1800$ K, and linear temperature sensitivity on the flow stress, i.e. $m = 1$. The applied thermal parameters are in line with modelling assumptions in several other studies on steels, e.g. [26, 27].

Table 1 Experimental material data and calibrated material parameters for the initiation pipe (I) and test pipes (1E, 2E).

		I	1E	2E
Exp. Data	*YS* [MPa]	470	490	530
	TS [MPa]	577	600	609
	CVN [J]	102	173	330
Hollomon	*A* [MPa]	802	833	800
	n [-]	0.100	0.099	0.077
Voce [MPa]	σ_0	470	492	531
	Q_1	216	223	170
	Θ_1	439	455	369
	Q_2	139	144	117
	Θ_2	3884	4052	3664
C-L [MPa]	W_C^{solid}	680	1050	1735
	W_C^{shell}	406	539	721

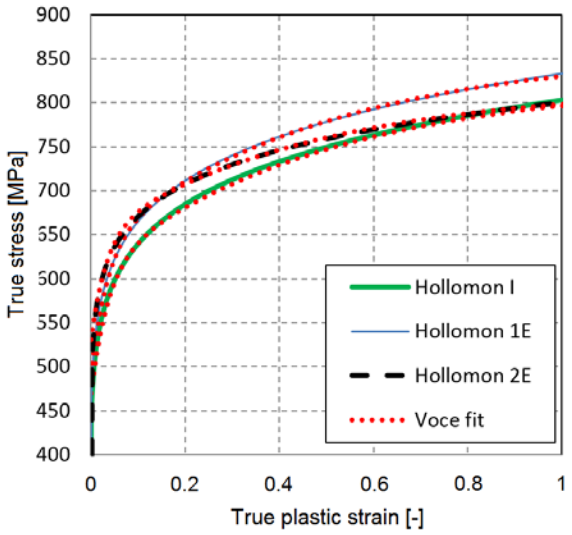

Figure 4 Estimated true stress - true plastic strain curves from the Hollomon equation and fitted Voce hardening rule.

Having estimated the flow stress parameters for each of the three pipe sections, the next step is to calibrate the fracture parameter W_C. To this end, the results from the CVN tests are applied. For each of the three materials, an FE model of the Charpy test is built and run with the material model described by Eq. (2) and (3). More details on the FE modelling of the Charpy test is found in [18]. The fracture parameter W_C is then adjusted until the CVN energy in the simulations is equal to the experimental value. The W_C values found from this analysis are valid for small (~0.3 mm) solid elements and are given as W_C^{solid} in Table 1. The Charpy tests on the high-toughness and the low-toughness pipes were instrumented [5], thus making a comparison with the FE simulations possible. As seen from Figure 5, the simulated force-displacement curves agree well with the experimental curves, although the peak force in the simulations is somewhat lower than in the tests. The results suggest that the applied material parameters for the I and 2E materials are representative of the steel materials used in the full-scale tests. The Charpy tests on the medium toughness material (1E) were not instrumented, and so a direct comparison with the FE force-displacement curve is not possible. However, as seen from Figure 5, the FE force-displacement curve for the medium toughness material is positioned between the curve for the low-toughness and the high-toughness material as expected.

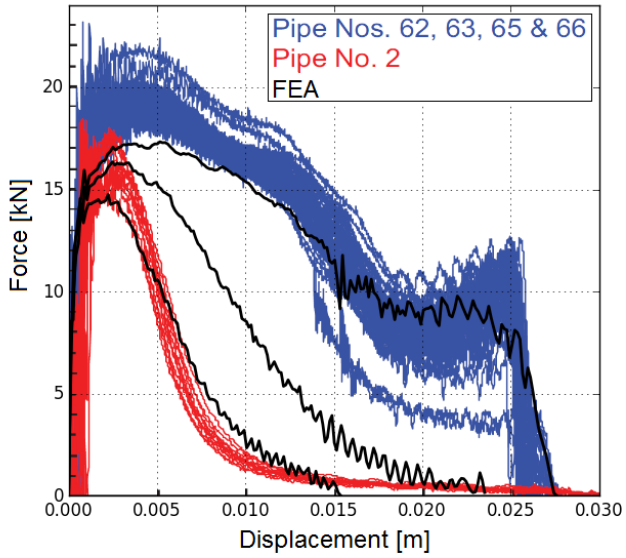

Figure 5 Force-displacement curves from CVN experiments and FE simulations based on CVN=102J, 173J and 330J. Pipe No 66 is the 2E pipe, Pipe No 2 is the initiation pipe (I).

Since the FE model of the full-scale test is using large shell elements along the crack-path, and not small solid elements as in the FE model of the Charpy test, scaling is needed to compensate for the difference in length scale. For each material, a simulation of a quasi-static, non-adiabatic virtual tensile test discretized by small solid elements was run up to onset of fracture as determined by W_C^{solid}. Then the nodal displacements of four nodes at the surface were collected. The nodes had an initial spacing of t x t/2, were t is the pipe wall thickness. The time histories of the nodal positions where then applied as boundary conditions in a shell element simulation to extract the scaled fracture parameter W_C^{shell}. Figure 6 shows the nodal positions in the initial configuration and at onset of fracture for the section I

material and close-up of the configuration at onset of fracture for all three materials. Similar scaling methods are applied in [18, 28, 29]. The final W_C^{shell} values are given in Table 1.

The backfill material was reported to be the native boulder clay while the cabling were padded with sand on the north side of the pipe [5]. Since no detailed information on the backfill material was provided, typical parameters for clay were applied in the M-C model in the full-scale simulation. An additional simulation using typical parameters for silt was also run on the shorter model to provide an idea of the sensitivity for the input parameters in the M-C model. The material parameters used for the clay and silt materials are compiled in Table 2. Here the density, ρ, the elastic shear modulus, G, and the Poisson ratio, ν, are taken from [30], while the friction angle, ϕ and the cohesion, C are found in [31]. Vermeer and de Borst [32] argued that the dilatation angle, ψ, is almost zero for clay and small <10° for silt.

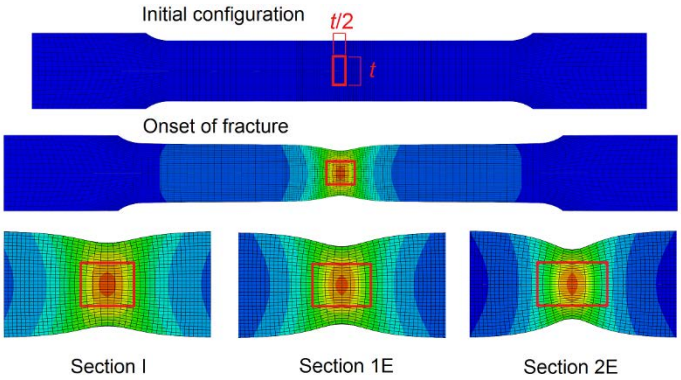

Figure 6 Tensile test simulations used for scaling of the fracture parameter at initial configuration and at onset of fracture. The positions of the four nodes used for the scaling is marked by a square. A close-up of the configuration at onset of fracture is shown for the three section materials.

Table 2 Parameters applied in the backfill material model

Material	ρ [kg/m^3]	G [MPa]	ν	φ	C [kPa]	ψ
Clay	1900	14.8	0.35	25°	8.0	0°
Silt	1750	3.8	0.30	35°	2.0	5°

RESULTS AND DISCUSSION

Full-scale simulation

Figure 7(a) shows the crack velocity as a function of crack length in the West and East directions in the experiment, and in the simulation of the East direction. Note that the first 0.58 m, which are used by the cutter, are included in the abscissa. The simulated crack-velocity agrees well with the experimental data, in sections I and 1E, but the FE-CFD model is conservative in section 2E and predicts a slower decrease in crack velocity than in the experiments. In the simulation of section I, the crack reaches a peak velocity of 170 m/s right after initiation before it continues with a velocity of ~135 m/s after approximately one OD length of propagation. The peak velocity can be interpreted as the result of a larger 'crack-driving force' stemming from two components:

(1) The closed geometry of the pipe at crack-initiation gives a larger area that the internal pressure applies on to generate stress at the crack-tip,
(2) The initial pressure is significantly higher than the saturation pressure.

After ~4 ms the crack has propagated ~1 OD and a full-bore opening has evolved, thus making point (1) above no longer valid. At the same time, the primary decompression wave has traveled away from the crack-tip and the pressure has dropped to the saturation pressure, thus making point (2) above no longer valid. The peak velocity is not observed in the experiment, but the use of explosives to initiate the crack propagation might influence the initial geometry of the pipe in contrast to the simulation where a perfectly cylindrical geometry is present at fracture initiation. The explosive charge might also provide other conditions at initiation that are not captured in the FE-CFD model. Another difference between simulation and experiment is the logging of the crack path; in the simulation, data is logged for each element that is deleted, i.e. for each 20 mm, while the distance between the timing wires in the test was 1.05 m, which might be too coarse to capture any initial peak velocity. The simulated steady-state velocity has a high-frequency noise with amplitude of ~5 m/s due to numerical differentiation. Apart from the high-frequency oscillations, the steady-state curve fluctuates at a lower frequency, between 125 m/s and 142 m/s in the initiation pipe, which is a somewhat smaller bound than the experimental scatter which is between 105 m/s and 132 m/s. As the crack enters section 1E, a distinct drop in crack velocity is observed in the simulation. A similar drop is seen in the experiment in the East and West directions. In the simulation, the crack reaches a new steady state velocity of 95-100 m/s, although the velocity is somewhat higher in the first part of the section. The experimental data in both directions show some scatter, but the steady-state velocity is deemed around 105 m/s in the last part of section 1E and 1W. In the experiment, the crack was arrested after propagating ~1 OD into sections 2E and 2W, while the crack propagates further into section 2E in the simulation. Figure 7(b) shows the pressure at the crack-tip as function of the crack-position from the FE-CFD simulation. While the pressure at the crack-tip is equal to the saturation pressure in sections I and 1E, a pressure drop is present at the crack-tip in section 2E indicating that the pressure wave is outrunning the propagating crack.

The FE-CFD model gives a good prediction of the crack propagation velocity in section 1E, but does not capture the rapid crack-arrest in section 2E. In the present case, EOS-CG [20] gives a saturation pressure of 86.4 barg which is 3 bar higher than Peng-Robinson, as illustrated in Figure 2. Cosham et al. [5] report a saturation pressure of 89 barg using GERG-2008 [19]. Including EOS-CG or GERG-2008 in the FE-CFD model would increase the crack velocity in section 1E, but would at the same time lead to a longer crack in section 2E. One possible explanation of the mismatch in simulated crack behavior in section 1E and 2E could be related to the fracture modelling. The

crack velocity is closely related to the fracture parameter; one increment in crack propagation is modelled as the deletion of one element, and this deletion occurs when the element is strained to a critical value determined by the fracture parameter. The larger the fracture parameter, the longer the time to strain the element to the critical value, and the slower the simulated propagation velocity. Determining a correct W_C^{shell} value is therefore crucial. The close relation between experimental and numerical force-displacement curves in Figure 5 indicates that the material model, including the fracture parameter for small solid elements, W_C^{solid}, represents the material crack-propagation behavior well at this length scale. Although the tensile test is appropriate to scale fracture initiation in a material with no existing crack-tip and which is exposed to significant necking, it may not be an appropriate choice to scale the fracture parameter for fracture propagation and arrest. From Table 1 it can be seen that the scaling depends on the ductility of the material; the $W_C^{shell} / W_C^{solid}$ ratio is decreasing from 0.60 in the least ductile section I material to 0.51 in the 1E material and 0.42 in the 2E material. For future work, the DWTT test will be used as a basis to scale the W_C^{shell} parameter as this test provides conditions much closer to the situation at the crack-tip in the full-scale test than a tensile test. Alternatively, the crack-path could be described using solid elements, but this approach is not practical due to higher computational costs.

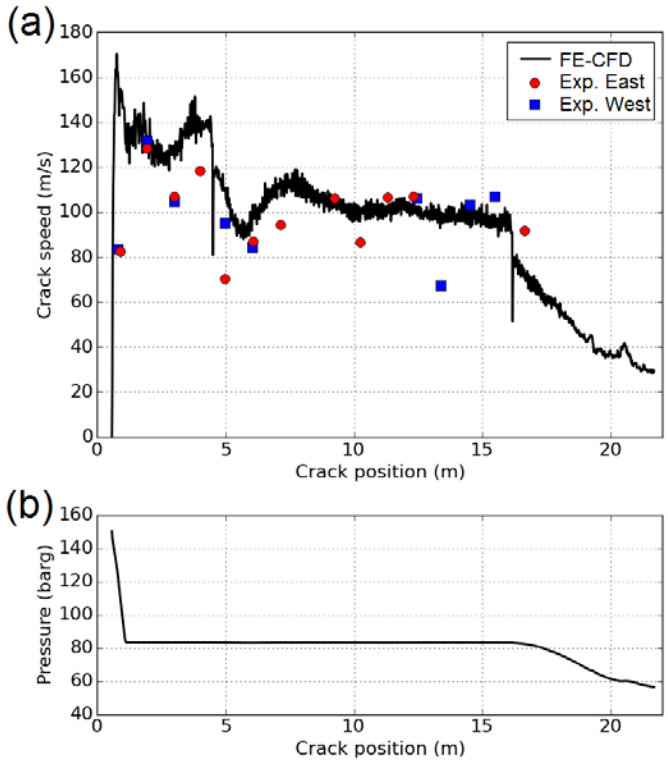

Figure 7 (a) Crack-speed as function of crack position in West and East direction in the experiment and in numerical analysis of the East direction. (b) Pressure at the crack-tip as function of the crack position in simulation.

The test pipe and the reservoirs had 9 pressure transducers in the East direction. Since the test sections 3E and the reservoirs are not included in the FE-CFD model, only the pressure at the first four pressure transducers are included, see Figure 8. The contours in Figure 8 represent the average pressure calculated from the CFD solver. Figure 8(a) shows the pipe 14 ms after initiation; the crack has propagated ~1 m in the initiation pipe, while the primary decompression wave has travelled into section 1E. Downstream the primary wave front, the pressure drops to the pressure plateau of 84.4 barg until a second pressure drop occurs at the crack-tip. Figure 8(b) shows the situation after 134 ms where the crack-tip has passed the position of pressure transducer P02. Here the primary decompression wave is outside of the model, a feature handled by the non-reflecting boundary condition applied at the end of section 2E. In the model, the pressure equals the saturation pressure upstream and at the crack tip, while downstream the crack tip, the pressure drops significantly over a few pipe diameters. Figure 8(c) shows the situation when the crack has entered 4.3 m into section 2E. Here, the second decompression wave have started to outrun the propagating crack, which again leads to a lower pressure at the crack-tip.

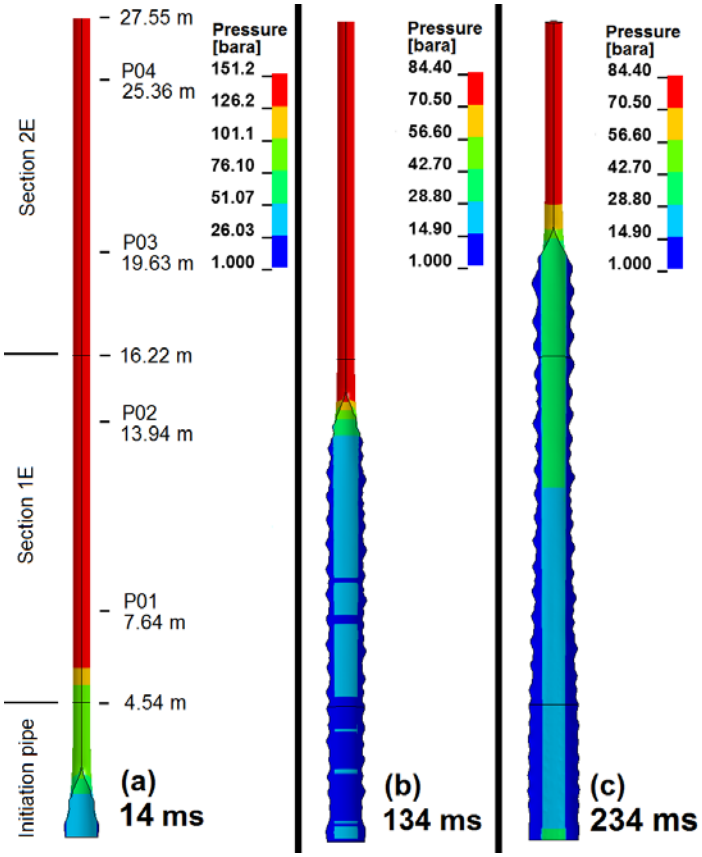

Figure 8 Crack propagation in simulation at (a) 34 ms, (b) 134 ms and (c) at 234 ms. The positions of the pressure transducers and the three sections are shown in (a).

The experimental and numerical pressures at the four pressure transducers are shown in Figure 9. The experimental curves have a sloping pressure plateau starting at ~90 barg and ending at ~82 barg and the pressure dropped immediately as the crack approached the pressure transducers P01 and P02 [5]. In the simulation, the sloping plateau is not reproduced due to the assumption of full equilibrium, and since in the model, after the saturation pressure has been reached, nothing influences the pressure until the arrival of the crack (for P01 and P02) or the second decompression wave (for P03 and P04). In the FE-CFD model calculation, the pressure plateau is approximately 1.5 bar higher than the final pressure plateau in the experiment. For the pressure transducer P02 the pressure drops approximately 17 ms later in the simulation than in the experiment. The discrepancy between the experimental and simulated pressure drop may be the combined effect of a somewhat slower crack propagation in the simulation of section 1E and a premature crack in the timing wire due to ovalization of the pipe prior to the arrival of the crack-tip [5]. In the experiment the crack did not pass pressure transducers P03 and P04. Due to the higher crack velocity in section 2E in the simulation, the second decompression wave passed P03 and P04 earlier, 15 ms and 40 ms respectively, than in the experiment.

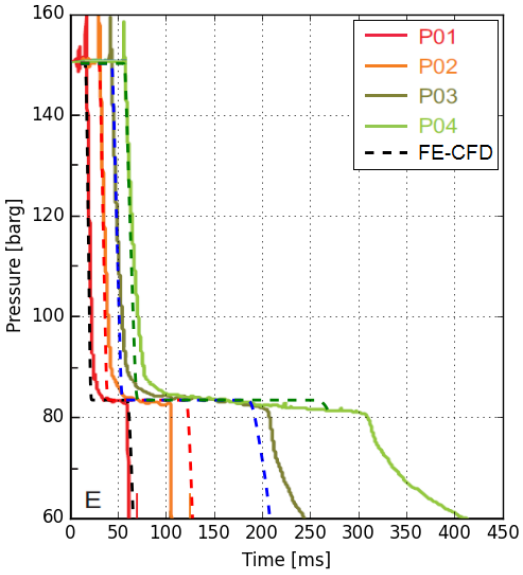

Figure 9 Pressure measured at the four first pressure transducers in the East direction and pressure collected from the FE-CFD simulation at the same locations.

The energy from the escaping fluid is transferred to kinetic energy and plastic dissipation of the pipe and the backfill as well as contact friction. The proportions between the different energy components are not easily measured in an experiment, but since the FE-CFD simulation captures the measured variables in the experiment well, it can give a good indication on how the energy is distributed. Table 3 gives the internal and kinetic energies of the pipe and the soil as well as the sliding energy which is related to the contact between the SPH particles and the shell elements at the end of the simulation. The internal energy variable contains the elastically stored energy and energies related to hourglassing, damping etc., but almost all the energy in this variable is energy dissipated in plastic deformation. The energy dissipated in the clay constitutes more than half of the total energy, while the kinetic energy in the pipe only constitutes 1% of the total energy. If there were no backfill, the energy would have been distributed differently and more energy would be transferred as kinetic energy in the pipe resulting in a higher crack speed. It is noted that out of the 18 MJ absorbed as internal energy in the pipe, 1.9 MJ is dissipated in the elements along the crack seam. This means that the energy dissipated in the crack modelling constitutes 2.5% of the total energy.

Table 3 Distribution of dissipated energy. In full-scale model, 'Short' model, 'Short' model with p_{sat}=89.3 barg and 'Short' model with silt backfill. In [MJ].

Energy Type	Full-scale	Short	p_{sat}=86.7	Silt
Total	77.4(100%)	42.6(100%)	47.1(100%)	26.9(100%)
Internal, Soil	45.7(59%)	24.4(57%)	27.0(57%)	13.3(50%)
Internal, Pipe	18.0(23%)	9.3(22%)	10.6(22%)	10.3(38%)
Kinetic, Soil	6.7 (9%)	4.6(11%)	5.1(11%)	1.5(5%)
Kinetic, Pipe	0.5(1%)	0.3(1%)	0.3(1%)	0.2(1%)
Sliding	6.5(8%)	3.9(9%)	4.1(9%)	1.7(6%)

Short model simulations

The crack-speed as function of crack position in the 'Short' model is compared with the result from the full-scale model in Figure 10. The data on the abscissa from the 'Short' model is adjusted so that the interface between section 1E and 2E are at the same position as in the full-scale model. As indicated in Figure 10(a), the crack velocity reach a peak of ~155 m/s due to the opening effect (the cutter is here 2 OD). When the crack leaves section 1E it holds a velocity of ~95 m/s and then drops to ~80 m/s as it enters section 2E. In the full-scale simulation a similar drop from ~95 m/s to ~77 m/s is observed. In both simulations the crack arrests in section 2E, although the 'Short' model has a somewhat higher velocity. This higher velocity is related to the pressure at the crack-tip, which is higher in the 'Short' model after the crack has entered section 2E, see Figure 10(b). The energy uptake distribution in the 'Short' model is similar to the full-scale model as seen from Table 3. In conclusion, the similarity between the results from the full-scale model and the 'Short' model are deemed sufficient for an initial parametric study, but more work must be conducted before a 'Short model approach' can be generally applied in validation activities based on large full-scale burst tests.

A simulation based on the 'Short' model was run with a saturation pressure of 89.3 barg, which is close to the upper bound of the experimentally determined saturation plateau in Figure 2. The saturation pressure was achieved by increasing the content of oxygen to 4 mol-% in the simulation. The increase of 6 bar in saturation pressure led to an increase in crack velocity

of ~20 m/s in both section 1E and section 2E as seen in Figure 10(a). As the crack entered section 2E, the velocity dropped to ~94 m/s and then decreased until arrest. The proportions of the absorbed energy are the same to those in the original 'Short' simulation as shown in Table 3, but the total energy is larger since more energy is released. The simulation suggests that the FE-CFD model gives a robust prediction of propagation and arrest with saturation pressures within the range of the experimentally determined saturation pressure plateau, but more detailed studies involving data from several crack-arrest experiments are needed to make a more general conclusion on the effect of the saturation pressure.

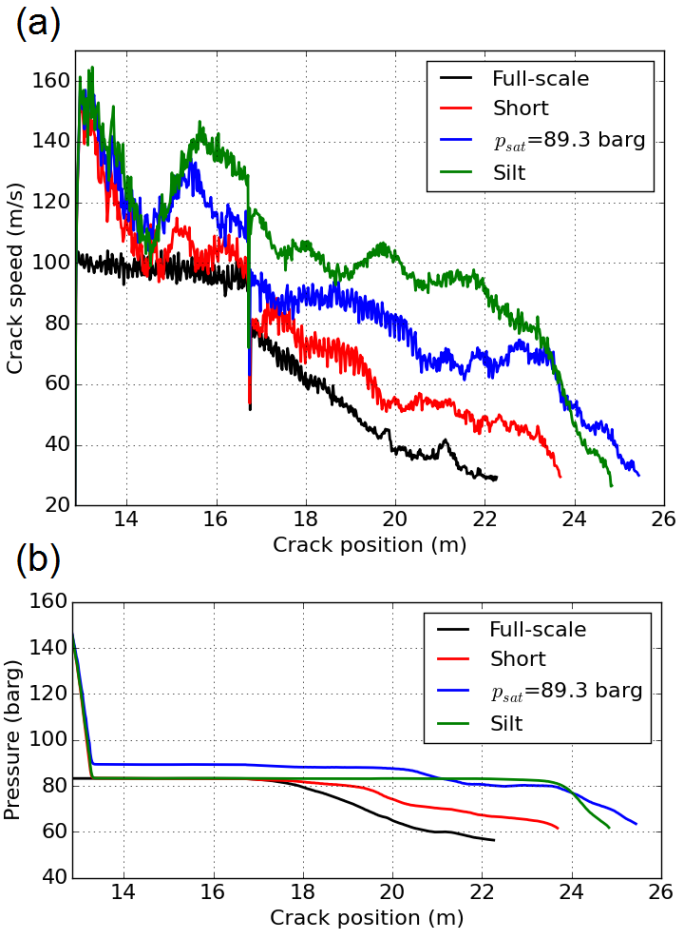

Figure 10 Results from short model full-scale model simulations. (a) Crack-speed as function of crack-position, and (b) pressure at crack tip as function of crack position.

The backfill was modelled with parameters suited for clay. To have an indication of the FE-CFD model's sensitivity to the backfill material, an additional simulation based on the 'Short' model was run using backfill parameters intended for silt, see Table 2. As shown in Figure 10(a), an increase in crack velocity of ~30 m/s is present in section 1E when using the silt backfill material. As the crack enters section 2E, the crack velocity drops from ~130 m/s to ~115 m/s. As seen in Figure 10(b), the pressure at the crack-tip stays at the saturation level the first ~6 m in section 2E before it starts to drop. In this first part of crack propagation in 2E, the crack velocity is still significantly higher than the velocity of the secondary decompression wave. The silt absorbs significantly less internal and kinetic energy (14.8 MJ) than the clay (29 MJ), see also Table 3, but this is partly due to the shorter timespan in this simulation (140 ms vs. ~170 ms). The shorter timespan also influences the sliding energy uptake. Another aspect is that the silt model has a lower shear strength which gives a lower traction on the outside of the flaring pipe walls, and so less resistance to the crack-driving force which stems from the pressure on the inside of the pipe. These results call for a more detailed sensitivity study on the backfill material model in the future.

CONCLUSIONS

A coupled FE-CFD model has been compared with existing data from a full-scale CO_2 fracture propagation test. In the experiment the crack goes through two pipe sections before it is arrested in the third. The results in terms of crack velocity and pressure decompression agree well between the numerical simulation and the experiment in the first two sections. However, the model predicts conservatively a slower drop in crack velocity in the third high-toughness pipe section. Using the DWTT test as an additional basis for fracture calibration might increase the accuracy of the model. The simulation indicates that more than half of the energy from the escaping fluid is transferred into internal energy in the surrounding clay and that less than 3% is dissipated along the crack path. An initial sensitivity study indicates that the FE-CFD model gives a robust prediction when saturation pressures within the range of the experimentally determined saturation pressure plateau are applied, and that the choice of backfill material parameters significantly influences the predicted propagation and arrest.

ACKNOWLEDGMENTS

The funding from the Norwegian CCS Research Centre, Centre for Environment-friendly Energy Research, is gratefully acknowledged.

REFERENCES

[1] Maxey, W. A. (1974). Fracture Initiation, Propagation and Arrest. 5th Symposium on Line Pipe Research. Huston, Texas.

[2] Leis, B. N., R. J. Eiber, L. Carlson and A. Gilroy-Scott (1998). Relationship between apparent (total) Charpy vee-notch toughness and the corresponding dynamic crack-propagation resistance ASME Paper No. IPC1998-2084 **2**.

[3] Wilkowski, G., W. Maxey and R. Eiber (1977). Use of a brittle notch DWTT specimen to predict fracture characteristics of line pipe steels. ASME 1977 Energy Technology Conference, Houston, Texas, Paper.

[4] Cosham, A., D. G. Jones, K. Armstrong, D. Allason and J. Barnett (2014). Analysis of two dense phase carbon dioxide full-scale fracture propagation tests ASME Paper No. IPC2014-33080.

[5] Cosham, A., D. G. Jones, K. Armstrong, D. Allason and J. Barnett (2016). Analysis of a Dense Phase Carbon Dioxide Full-Scale Fracture Propagation Test in 24 Inch Diameter Pipe ASME Paper No. IPC2016-64456(50275).
[6] ISO/TC 265 (2016). ISO 27913:2016 Carbon dioxide capture, transportation and geological storage -Pipeline transportation systems.
[7] DNV-GL (2017). DNVGL-RP-F104 Design and operation of carbon dioxide pipelines.
[8] Biagio, M. D., A. Lucci, E. Mecozzi and C. M. Spinelli (2017). Fracture Propagation Prevention on CO2 Pipelines: Full Scale Experimental Testing and Verification Approach. Pipeline Technology Conference. Berlin.
[9] Mahgerefteh, H., S. Brown and G. Denton (2012). Modelling the impact of stream impurities on ductile fractures in CO2 pipelines Chemical Engineering Science **74**: 200-210.
[10] Scheider, I., A. Nonn, A. Völling, A. Mondry and C. Kalwa (2014). A Damage Mechanics based Evaluation of Dynamic Fracture Resistance in Gas Pipelines Procedia Materials Science **3**: 1956-1964.
[11] Nonn, A. and C. Kalwa (2013). Analysis of dynamic ductile fracture propagation in pipeline steels: a damage-mechanics' approach. 6th International Pipeline Technology Conference.
[12] Shim, D.-J., G. Wilkowski, D. Rudland, B. Rothwell and J. Merritt (2008). Numerical Simulation of Dynamic Ductile Fracture Propagation Using Cohesive Zone Modeling ASME Paper No. IPC2008-64049(48593): 21-28.
[13] O'Donoghue, P. E., M. F. Kanninen, C. P. Leung, G. Demofonti and S. Venzi (1997). The development and validation of a dynamic fracture propagation model for gas transmission pipelines International Journal of Pressure Vessels and Piping **70**(1): 11-25.
[14] Yang, X. B., Z. Zhuang, X. C. You, Y. R. Feng, C. Y. Huo and C. J. Zhuang (2008). Dynamic fracture study by an experiment/simulation method for rich gas transmission X80 steel pipelines Engineering Fracture Mechanics **75**(18): 5018-5028.
[15] Shibanuma, K., T. Hosoe, H. Nakai, A. Morita and S. Aihara (2017). A model to evaluate unstable ductile crack arrestability of offshore pipeline Engineering Fracture Mechanics **178**: 126-147.
[16] Nordhagen, H. O., S. Kragset, T. Berstad, A. Morin, C. Dørum and S. T. Munkejord (2012). A new coupled fluid–structure modeling methodology for running ductile fracture Computers & Structures **94-95**: 13-21.
[17] Aursand, E., S. Dumoulin, M. Hammer, H. I. Lange, A. Morin, S. T. Munkejord and H. O. Nordhagen (2016). Fracture propagation control in CO2 pipelines: Validation of a coupled fluid–structure model Engineering Structures **123**: 192-212.
[18] Nordhagen, H. O., S. T. Munkejord, M. Hammer, G. Gruben, M. Fourmeau and S. Dumoulin (2017). A fracture-propagation-control model for pipelines transporting CO2-rich mixtures including a new method for material-model calibration Engineering Structures **143**(Supplement C): 245-260.
[19] Kunz, O. and W. Wagner (2012). The GERG-2008 Wide-Range Equation of State for Natural Gases and Other Mixtures: An Expansion of GERG-2004 Journal of Chemical & Engineering Data **57**(11): 3032-3091.
[20] Gernert, J. and R. Span (2016). EOS–CG: A Helmholtz energy mixture model for humid gases and CCS mixtures The Journal of Chemical Thermodynamics **93**: 274-293.
[21] Peng, D. Y. and D. B. Robinson (1976). A New Two-Constant Equation of State Industrial and Engineering Chemistry Fundamentals **15**(1): 59-64.
[22] LSTC (2015). LS-DYNA KEYWORD USER'S MANUAL. LS-DYNA R8.0 03/23/15 (r:6319). Livermore, California 94551-0712, Livermore Software Technology Corporation.
[23] Munkejord, S. T. and M. Hammer (2015). Depressurization of CO_2-rich mixtures in pipes: Two-phase flow modelling and comparison with experiments International Journal of Greenhouse Gas Control **37**(0): 398-411.
[24] Hammer, M., Å. Ervik and S. T. Munkejord (2013). Method Using a Density–Energy State Function with a Reference Equation of State for Fluid-Dynamics Simulation of Vapor–Liquid–Solid Carbon Dioxide Industrial & Engineering Chemistry Research **52**(29): 9965-9978.
[25] Liessem, A., G. Knauf and S. Zimmermann (2007). Strain Based Design—What the Contribution of a Pipe Manufacturer Can Be, International Society of Offshore and Polar Engineers.
[26] Børvik, T., O. S. Hopperstad, T. Berstad and M. Langseth (2001). A computational model of viscoplasticity and ductile damage for impact and penetration European Journal of Mechanics - A/Solids **20**(5): 685-712.
[27] Børvik, T., S. Dey and A. H. Clausen (2009). Perforation resistance of five different high-strength steel plates subjected to small-arms projectiles International Journal of Impact Engineering **36**(7): 948-964.
[28] Gruben, G., S. Sølvernes, T. Berstad, D. Morin, O. S. Hopperstad and M. Langseth (2017). Low-velocity impact behaviour and failure of stiffened steel plates Marine Structures **54**: 73-91.
[29] Morin, D., B. L. Kaarstad, B. Skajaa, O. S. Hopperstad and M. Langseth (2017). Testing and modelling of stiffened aluminium panels subjected to quasi-static and low-velocity impact loading International Journal of Impact Engineering **110**: 97-111.
[30] Subramanian, N. (2016). Design of Steel Structures, Oxford University Press.
[31] Ortiz, J. M. R., J. s. S. Gesta and C. O. Mazo (1989). Curso Aplicado de Cimentaciones. Madrid, COLEGIO OFICIAL de ARQUITECTOS de MADRID.
[32] Vermeer, P. A. and R. d. Borst (1984). Non-associated plasticity for soil, concrete and rock Heron **29**: 1-64.

